Journal of Alloys and Compounds 1044 (2025) 184627

Contents lists available at ScienceDirect

Journal of Alloys and Compounds

journal homepage: www.elsevier.com/locate/jalcom

Nb microalloying enhances the amorphous forming ability and soft magnetic properties of high B_s Fe-based nanocrystalline alloys

Yanzhou Fan, Changlong Jin, Min Wang, Jifeng Zhou, Jinhong Fu, Dong Li, Qiang Luo, Zhijun Guo *, Baolong Shen *

School of Materials Science and Engineering, Jiangsu Key Laboratory for Advanced Metallic Materials, Southeast University, Nanjing 211189, China

ARTICLE INFO

Keywords:
Fe-based nanocrystalline alloys
Amorphous forming ability
Nb microalloying
Refined grain size
Superior soft magnetic properties

ABSTRACT

Fe-based nanocrystalline alloys with high saturation magnetic flux density (B_s) are essential for enhancing the power density of electrical and electronic devices and have attracted increasing attention in recent years. However, their limited amorphous forming ability (AFA) and stringent annealing requirement hinder large-scale industrial applications. In this study, we systematically investigated the effects of Nb content on the thermal stability, AFA, microstructural evolution and soft-magnetic properties of $Fe_{76.3-x}Si_9B_{10}P_4Cu_{0.7}Nb_x$ (x = 0, 0.5, 1.0, 1.5 and 2.0) nanocrystalline alloys. The results reveal that Nb microalloying can effectively broaden the heat treatment window and expand the supercooled liquid region, facilitating industrial processing. Notably, the average grain size was significantly reduced from 35 nm (Nb0) to 15 nm (Nb1.5). Meanwhile, the crystallization volume fraction increased from 34.6 % (Nb0) to 55.5 % (Nb1.5), and the thickness of the intergranular amorphous layer decreased markedly from 14.9 nm (Nb0) to 3.3 nm (Nb1.5). Consequently, the Nb1.5 alloy exhibits superior soft magnetic performance, achieving a high B_s of 1.36 T, an effective permeability (μ_e) of 19400, low coercivity (H_c) of 1.75 A/m, and low core loss P_{cm} (0.2 T, 20 kHz) of 4.94 W/kg. This Nb microalloying strategy provides an effective approach for optimizing Fe-based nanocrystalline alloys, making the Nb1.5 alloy a promising candidate for energy-efficient magnetic device applications.

1. Introduction

Soft magnetic materials play a crucial role in energy transmission and conversion within electrical and electronic systems [1]. In response to the escalating global energy crisis and stringent emission reduction requirements, modern electronic devices are undergoing rapid advancements towards miniaturization, higher operating frequencies, and enhanced energy efficiency [2,3]. To achieve these critical demands, the development of novel soft magnetic materials with superior comprehensive properties such as high B_s, low H_c, and low P_{cm} is imperative.

Fe-based nanocrystalline alloys have emerged as the most promising candidate materials to address this challenge due to their exceptional soft magnetic properties [4,5]. Among them, Finemet alloys have achieved large-scale commercial success, primarily due to their excellent manufacturability [6]. However, the relatively low B_s (~1.24 T), resulting from a high Nb content and reduced Fe content, limits their application in high power density and miniaturized devices [7,8]. To enhance B_s, Makino et al. [9,10] developed FeSiBPCu nanocrystalline alloys in 2009, achieving B_s value in a range of 1.8–1.85 T. However, their low AFA and stringent crystallization conditions hinder widespread application [11–13]. Consequently, achieving a synergistic balance of high B_s, high AFA and superior soft magnetic properties in Fe-based nanocrystalline alloys remains a significant challenge.

Studies have shown that the strategic addition of transition metals can effectively suppress α-Fe nanocrystals growth while enhancing the soft magnetic properties of FeSiBCu[14] and FeSiBPCu [13,15] alloys. Empirical evidence suggests that large atomic-sized transition metals such as Zr, Nb, Mo, Mn and Cr promote the formation of amorphous structures [16–19]. Amongst these, Zr is the most effective in enhancing AFA, followed sequentially by Nb, Mo, Mn, Cr [20]. However, the high reactivity of Zr with oxygen complicates the fabrication of Zr containing Fe-based amorphous/nanocrystalline alloys, restricting their practical application to laboratory-scale research [21]. Additionally, antiferromagnetic elements such as Mn and Cr suppress the ferromagnetic interactions in Fe-based amorphous alloys, leading to a pronounced reduction in B_s[22]. Meanwhile, Chang et al. [13,23] reported that

---

* Corresponding authors.
E-mail addresses: zj-guo@seu.edu.cn (Z. Guo), blshen@seu.edu.cn (B. Shen).

https://doi.org/10.1016/j.jallcom.2025.184627
Received 7 July 2025; Received in revised form 21 October 2025; Accepted 23 October 2025

incorporating 1 at% Nb effectively broadens the optimal annealing temperature window and prolongs the thermal stability of high B_s nanocrystalline alloy $Fe_{83}Si_4B_{10}P_2Cu_1$. The results show that adding Nb can increase the activation energy for grain growth and refine the grain size, where $Fe_{82}Si_4B_{10}P_2Cu_1Nb_1$ alloy exhibits the lowest H_c and the highest μ_e[23]. Therefore, Nb is considered the most suitable candidate for optimizing the microstructure and magnetic performance of Fe-based nanocrystalline alloys.

According to our previous work, we developed $Fe_{72}Si_9B_{10}P_2C_2Nb_5$ amorphous alloy with high AFA, which can be used to prepare amorphous powders. However, B_s was found to be low due to the high Nb content in the alloy [24]. It has been widely reported that P atoms in the amorphous matrix separate from Fe atoms and coordinate with Cu atoms during annealing due to the negative mixing enthalpy between Cu and P (-9 kJ/mol). These separated Cu and P atoms tend to form CuP clusters, which can serve as heterogeneous nucleation sites for α-Fe, ultimately refining the grains [25]. Therefore, based on the above alloy composition, the effect of trace Nb addition on the thermal stability, AFA and soft-magnetic properties of $Fe_{76.3\text{-}x}Si_9B_{10}P_4Cu_{0.7}Nb_x$ nanocrystalline alloys was investigated. Furthermore, we analyzed the microstructural evolution and magnetic domain behavior to elucidate the underlying structural mechanisms governing these improvements. Our findings provide valuable insights into the design of Fe-based nanocrystalline alloys with high B_s and outstanding soft magnetic properties, facilitating the advancement of next-generation energy-efficient magnetic devices.

2. Experimental procedure

Alloy ingots with nominal compositions of $Fe_{76.3\text{-}x}Si_9B_{10}P_4Cu_{0.7}Nb_x$ (x = 0, 0.5, 1.0, 1.5 and 2.0 at%; hereafter denoted as Nb0, Nb0.5, Nb1.0, Nb1.5 and Nb2.0, respectively) were synthesized *via* induction melting in an argon atmosphere. The raw materials included high-purity Fe (99.99 wt%), Si (99.999 wt%), B (99.99 wt%), Cu (99.99 wt%), Nb (99.99 wt%), and pre-alloys of Fe-P (26.4 wt% P). Ribbon samples with a width of ~ 1 mm and a thickness of ~ 22 μm were fabricated by a single roll melt spinning technology, with a wheel speed of about 40 m/s. The thermal properties, including curie temperature (T_C), glass transition temperature (T_g), primary crystallization temperature (T_{x1}) and secondary crystallization temperature (T_{x2}), were determined *via* differential scanning calorimeter (DSC, Netzsch 404 F3) under high purity argon flow at heating rate of 20 °C/min. The as-quenched ribbons were annealed at a temperature ranging from 480 °C to 560 °C for 20 min under high vacuum conditions to optimize their magnetic performance. The microstructure was characterized by X-ray diffraction (XRD, Bruker D8-Discover) with Cu-Kα radiation and transmission electron microscopy (TEM, Talos F200X). Magnetic properties, including B_s, μ_e, H_c, and core loss P_{cm} were measured using a vibrating sample magnetometer (VSM, LakeShore 7407) under a maximum applied field of 800 kA/m, an impedance analyzer (Keysight, E4990A) under a field of 1 A/m, a DC B-H loop tracer (Riken BHS-40) under a maximum applied field of 1 kA/m, and an AC B-H loop tracer (Riken AC BH-100 K) respectively. Magnetic domain structures were visualized using a magneto-optical Kerr microscope (Evico Magnetics GmbH, em-Kerr-highres).

3. Results and discussion

3.1. Thermal analysis and amorphous forming ability

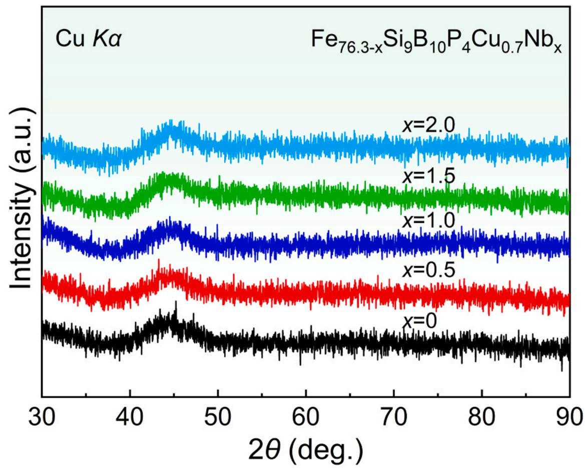

Fig. 1. XRD patterns of as-quenched $Fe_{76.3\text{-}x}Si_9B_{10}P_4Cu_{0.7}Nb_x$ (x = 0, 0.5, 1.0, 1.5 and 2.0) alloy ribbons.

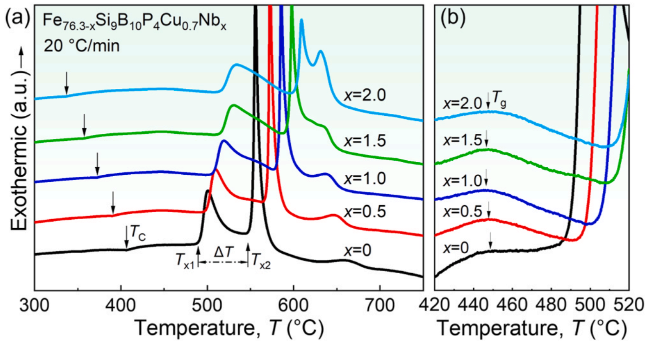

Fig. 2. (a) DSC curves of as-quenched $Fe_{76.3\text{-}x}Si_9B_{10}P_4Cu_{0.7}Nb_x$ (x = 0, 0.5, 1.0, 1.5 and 2.0) alloy ribbons recorded at a heating rate of 20 °C/min. (b) magnified DSC curves highlighting the supercooled liquid region.

Fig. 1 shows the XRD patterns of the as-quenched $Fe_{76.3\text{-}x}Si_9B_{10}P_4Cu_{0.7}Nb_x$ (x = 0, 0.5, 1.0, 1.5 and 2.0) alloy ribbons with varying Nb content. For all compositions, the diffraction patterns exhibit broad halos centered around 2θ = 45°, with no sharp peaks corresponding to crystalline phases, confirming that all ribbons possess a fully amorphous structure. Fig. 2**(a)** displays the DSC curves of as-quenched $Fe_{76.3\text{-}x}Si_9B_{10}P_4Cu_{0.7}Nb_x$ alloy ribbons measured at a 20 °C/min heating rate under an argon atmosphere. Three exothermic peaks in all compositions indicate a multiple-step crystallization process. The onset crystallization temperature (T_{x1}) of the first peak corresponds to the precipitation of bcc-Fe(Si) phase, whereas the second (T_{x2}) and third peaks correspond to the crystallization of $Fe_3(B, P)$ and Fe_2B phases, respectively [26]. As Nb content increases, both T_{x1} and T_{x2} shift to higher temperatures and the temperature interval ($\Delta T = T_{x2}\text{-}T_{x1}$) expands. Notably, ΔT increases from 59 °C for Nb0 to 86.5 °C for Nb2. It is well established that a large ΔT promotes the formation of a homogeneous α-Fe(Si) phase while suppressing the precipitation of the Fe(B, P) compounds [23,27]. This suggests that Nb addition enhances the thermal stability of amorphous phase and facilitates superior soft magnetic properties. Fig. 2**(b)** presents the magnified DSC curves highlighting the supercooled liquid region. The endothermic peak corresponding to the T_g is observed in all alloys, although it is less distinct for the Nb0 sample. The width of the supercooled liquid region ($\Delta T_x = T_{x1}\text{-}T_g$) increases from 43 °C for Nb0 to 70 °C for Nb1.5. Beyond 1.5 at% Nb, ΔT_x remains nearly constant. A large ΔT_x indicates superior thermal stability against crystallization, which means the Nb-containing alloys exhibit a high AFA [28]. It is worth noting that although the Finemet alloy exhibits excellent soft magnetic properties, it does not exhibit a supercooled liquid region due to its high Cu content, implying a low AFA. Consequently, it is mostly used in ribbon form. In contrast, the Nb1.5 alloy exhibits a wide supercooled liquid region, implying a high AFA. This high AFA facilitates the preparation of amorphous powders via atomization, which is crucial for the fabrication of nanocrystalline magnetic powder cores with the excellent high-frequency properties required for next-generation wide-bandgap semiconductor applications.

The topological parameter atomic mismatch (δ) and thermodynamic parameter mixing enthalpy (ΔH_{mix}) are widely employed to evaluate AFA. A higher δ among alloying elements promotes dense atomic packing, which hinders atomic diffusion and enhances amorphization. Additionally, a more negative ΔH_{mix} favors the stabilization of supercooled liquids state, further improving AFA. The atomic mismatch parameter δ is defined as follows [29]:

$$\delta = \sqrt{\sum_{i=1}^{n} c_i \left[1 - r_i \Big/ \left(\sum_{j=1}^{n} c_j r_j\right)\right]^2} \qquad (1)$$

where n is the number of elements in the alloy, c_i and c_j denote atomic percentages, and r_i and r_j represent the atomic radii of the constituent elements.

Similarly, the ΔH_{mix} is given by [29]:

$$\Delta H_{mix} = \sum_{i=1, j>i}^{n} 4\Delta H_{AB}^{mix} c_i c_j \qquad (2)$$

where ΔH_{AB}^{mix} is the mixing enthalpy of binary alloy with equal atomic ratio of elements A and B. Table1 summarizes the calculated δ and ΔH_{mix} values for $Fe_{76.3\text{-}x}Si_9B_{10}P_4Cu_{0.7}Nb_x$. As Nb content increases, δ gradually increases and ΔH_{mix} becomes more negative, both of which enhance AFA. This enhancement contributes to a more uniform amorphous structure, which facilitates the preparation of high-performance soft magnetic materials.

3.2. Soft magnetic properties

The temperature dependence of coercivity (H_c) for $Fe_{76.3\text{-}x}Si_9B_{10}P_4Cu_{0.7}Nb_x$ ribbons annealed for 20 min is presented in Fig. 3. As the annealing temperature increases, H_c initially decreases and subsequently rises. In alloys with x = 0 and 0.5, there is a pronounced increase in H_c at 520 °C. In contrast, for alloys with x = 1.5 and x = 2.0, H_c remains relatively stable and maintains a low value when annealed between 480 °C and 520 °C. Furthermore, as Nb content increases, H_c at the optimum annealing temperature decreases sharply from 9.6 A/m for Nb0 alloy to 1.75 A/m for Nb1.5 alloy. When the Nb content is further increased to 2.0 at%, H_c decreases slightly to 1.51 A/m. Though the H_c of the Nb1.5 and Nb2 alloys is fairly good, it is still higher than that of the Finemet alloy (0.53 A/m). This difference is attributed to the higher Cu content in Finemet, which promotes the nucleation of α-Fe(Si) nanocrystals and results in a much higher crystallization volume fraction (70–80 vol%) [4,30]. Fig. 4 displays the hysteresis loops of $Fe_{76.3\text{-}x}Si_9B_{10}P_4Cu_{0.7}Nb_x$ alloy ribbons annealed at optimized annealing temperatures. All alloys exhibit characteristic soft magnetic behavior, achieving rapid magnetic saturation under a small applied magnetic field. As shown in the inset, the B_s decreases monotonously with increasing Nb content, from 1.48 T (Nb0) to 1.32 T (Nb2.0), yet it remains at a relatively high level overall compared to the commercial Finemet alloy (1.24 T) [31]. The frequency-dependent μ_e of $Fe_{76.3\text{-}x}Si_9B_{10}P_4Cu_{0.7}Nb_x$ alloy ribbons, annealed at optimized temperatures, is shown in Fig. 5. μ_e exhibits a gradual decline in the low-frequency region, followed by a sharp decrease beyond 30 kHz. The size resonance phenomenon occurs near 30 kHz, which may be related to the resonance of the wavelength of the applied electromagnetic field being close to the thickness of the alloy sample, and similar results have been reported in

Table1
Calculated atomic mismatch parameters (δ) and mixing enthalpies (ΔH_{mix}) for $Fe_{76.3\text{-}x}Si_9B_{10}P_4Cu_{0.7}Nb_x$.

$Fe_{76.3\text{-}x}Si_9B_{10}P_4Cu_{0.7}Nb_x$	δ	ΔH_{mix} (kJ/mol)
x = 0	0.1083	−23.02
x = 0.5	0.1092	−23.40
x = 1.0	0.1100	−23.78
x = 1.5	0.1109	−24.15
x = 2.0	0.1117	−24.52

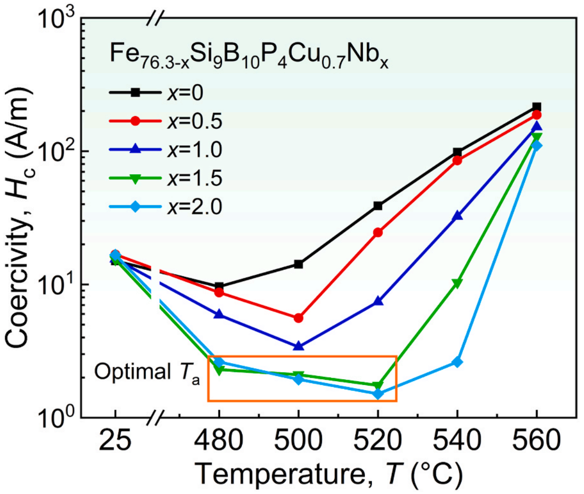

Fig. 3. Variation of H_c as a function of annealing temperature for $Fe_{76.3\text{-}x}Si_9B_{10}P_4Cu_{0.7}Nb_x$ (x = 0, 0.5, 1.0, 1.5 and 2.0) ribbons subjected to 20 min annealing.

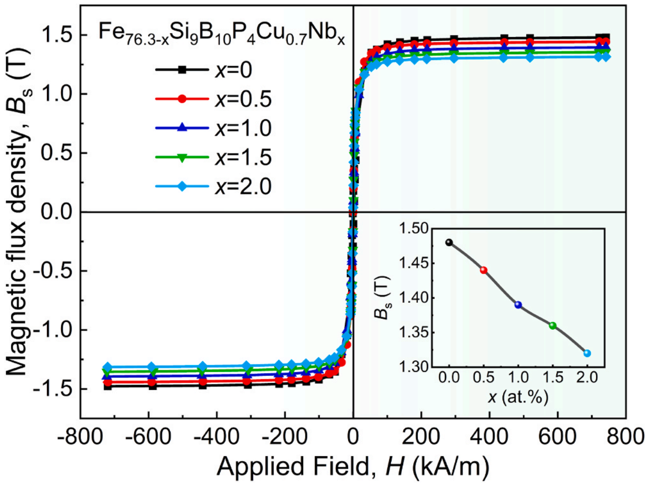

Fig. 4. Hysteresis loops of $Fe_{76.3\text{-}x}Si_9B_{10}P_4Cu_{0.7}Nb_x$ (x = 0, 0.5, 1.0, 1.5 and 2.0) alloy ribbons annealed at optimized temperatures.

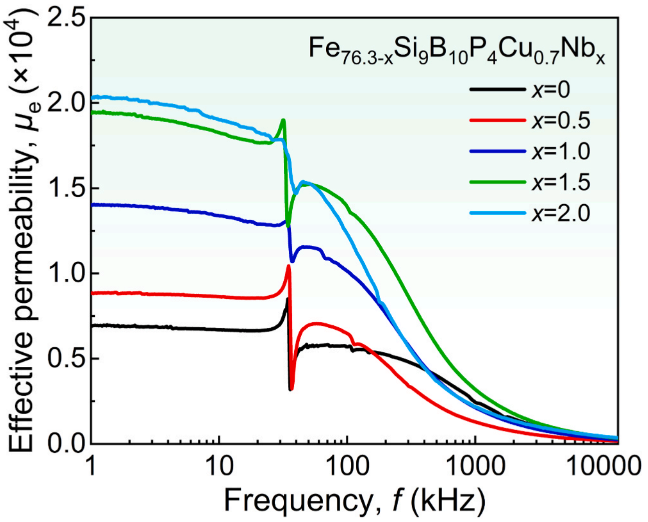

Fig. 5. Effective permeability (μ_e) of $Fe_{76.3\text{-}x}Si_9B_{10}P_4Cu_{0.7}Nb_x$ (x = 0, 0.5, 1.0, 1.5 and 2.0) alloy ribbons annealed at optimized temperatures.

other nanocrystalline alloys [32,33]. Additionally, μ_e at 1 kHz increases with Nb content, this trend inversely correlates with that of H_c, reinforcing the role of Nb in optimizing soft magnetic properties. Fig. 6 displays the P_{cm} at 0.2 T with respect to the frequency of $Fe_{76.3\text{-}x}Si_9B_{10}P_4Cu_{0.7}Nb_x$ (x = 0, 0.5, 1.0, 1.5, and 2.0) nanocrystalline alloys subjected to optimal treatments. The P_{cm} of all samples increases with increasing frequency and decreases significantly when Nb content is more than 1.0 at%. The P_{cm} under the condition of 0.2 T and 20 kHz decreases from 7.38 W/kg (Nb0) to 4.58–4.94 W/kg (Nb1.5 and Nb2.0). Considering the overall magnetic properties of Fe-based nanocrystalline alloys, the addition of 1.5 at% Nb is the optimal content for microalloying.

3.3. Microstructural evolution

Soft magnetic properties of nanocrystalline alloys are closely related to their microstructures. Fig. 7 shows the XRD patterns of $Fe_{76.3\text{-}x}Si_9B_{10}P_4Cu_{0.7}Nb_x$ alloy ribbons annealed at optimized temperatures. All samples exhibit three distinct crystallization peaks at approximately $2\theta = 45^\circ$, 65.6°, and 82.9°, corresponding to (110), (200) and (211) planes of the α-Fe(Si) phase, respectively. Fig. 8 shows the effect of Nb content on the crystallization volume fraction (V_{cr}) of α-Fe(Si) phase and the thickness of the intergranular amorphous layer (Λ) in $Fe_{76.3\text{-}x}Si_9B_{10}P_4Cu_{0.7}Nb_x$ (x = 0, 0.5, 1.0, 1.5 and 2.0) alloy ribbons annealed at optimized temperatures. The V_{cr} and Λ can be calculated using the equations [34,35]:

$$V_{cr} = \frac{I_{cr}}{I_{cr} + I_{am}} \tag{3}$$

$$\Lambda = D\left[(1/V_{cr})^{1/3} - 1\right] \tag{4}$$

where I_{cr} and I_{am} are the diffraction intensities of the crystalline and amorphous peak, respectively, and the diffraction intensity is equal to the area of the diffraction peak. D is the average grain size of α-Fe(Si) phase, which can be estimated using transmission electron microscopy (TEM). The result is shown in Fig. 8 and Table 2. It can be seen that as the Nb content increases, the V_{cr} gradually increases. At the same time, the Λ significantly decreases from 14.9 nm in the Nb0 alloy to 3.3 nm in the Nb1.5 alloy, and further decreases to 2.8 nm as the Nb content increases. It can be seen from Fig. 2 that the addition of Nb delays the crystallization of $Fe_3(B,P)$, thereby increasing the optimum annealing temperature for H_c from 480 °C to 520 °C, which also results in an increase in V_{cr}. In addition, the grain size can be significantly refined by adding trace amounts of Nb. The decrease in D and increase in V_{cr} are advantageous for reducing Λ and improving soft magnetic properties.

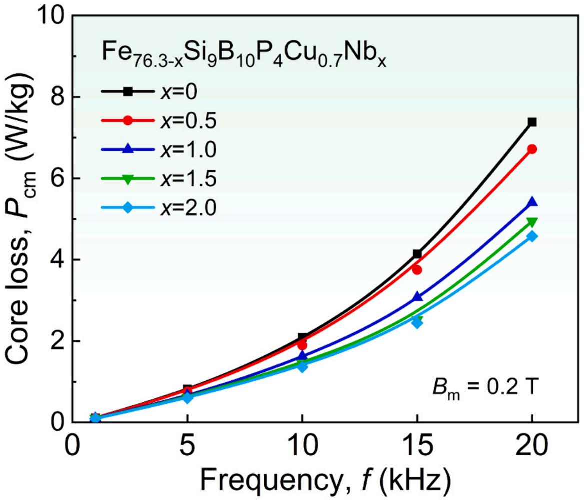

Fig. 6. Frequency dependent of P_{cm} measured at $B_m = 0.2$ T of $Fe_{76.3\text{-}x}Si_9B_{10}P_4Cu_{0.7}Nb_x$ (x = 0, 0.5, 1.0, 1.5 and 2.0) alloy ribbons annealed at optimized temperatures.

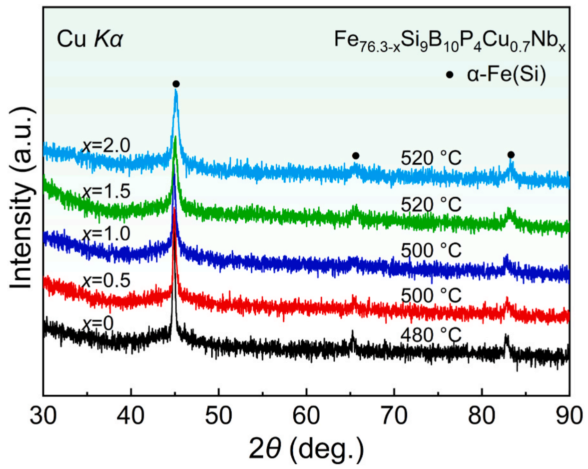

Fig. 7. XRD patterns of $Fe_{76.3\text{-}x}Si_9B_{10}P_4Cu_{0.7}Nb_x$ (x = 0, 0.5, 1.0, 1.5 and 2.0) alloy ribbons annealed at optimized temperatures.

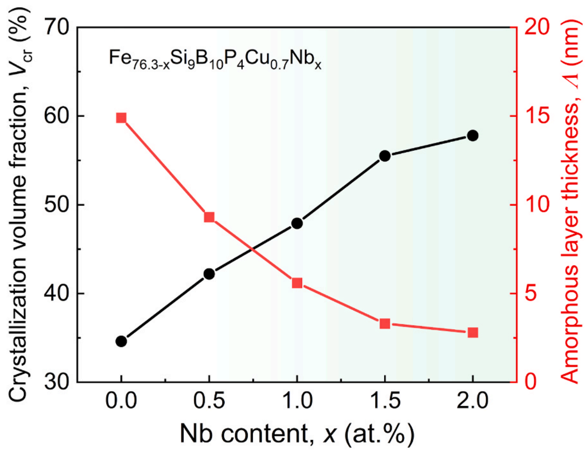

Fig. 8. The effect of Nb content on the crystallization volume fraction (V_{cr}) of α-Fe(Si) phase and the thickness of the intergranular amorphous layer (Λ) in $Fe_{76.3\text{-}x}Si_9B_{10}P_4Cu_{0.7}Nb_x$ (x = 0, 0.5, 1.0, 1.5 and 2.0) alloy ribbons annealed at optimized temperatures.

Table2

Average grain size (D), crystalline volume fraction (V_{cr}), and the thickness of intergranular amorphous layer (Λ) in $Fe_{76.3\text{-}x}Si_9B_{10}P_4Cu_{0.7}Nb_x$ alloy ribbons annealed at optimized temperatures.

$Fe_{76.3\text{-}x}Si_9B_{10}P_4Cu_{0.7}Nb_x$	D (nm)	V_{cr} (%)	Λ (nm)
x = 0	35	34.6	14.9
x = 0.5	28	42.2	9.3
x = 1.0	20	47.9	5.6
x = 1.5	15	55.5	3.3
x = 2.0	14	57.8	2.8

To further investigate the effect of Nb addition on the microstructure, Nb0 and Nb1.5 alloys were analyzed by TEM. As shown in Fig. 9**(a-c)**, Nb0 alloy exhibits a sparse distribution of coarse, square-shaped nanograins, and the average grain size is 35 nm. Selected-area electron diffraction (SAED) patterns confirm that these nanocrystals are α-Fe phases (Fig. 9**(b)**). In contrast, Nb1.5 exhibits a significantly different microstructure compared to the Nb0 alloy. Nb1.5 possesses an ultrafine nanocrystalline-amorphous dual-phase structure, with nanocrystalline

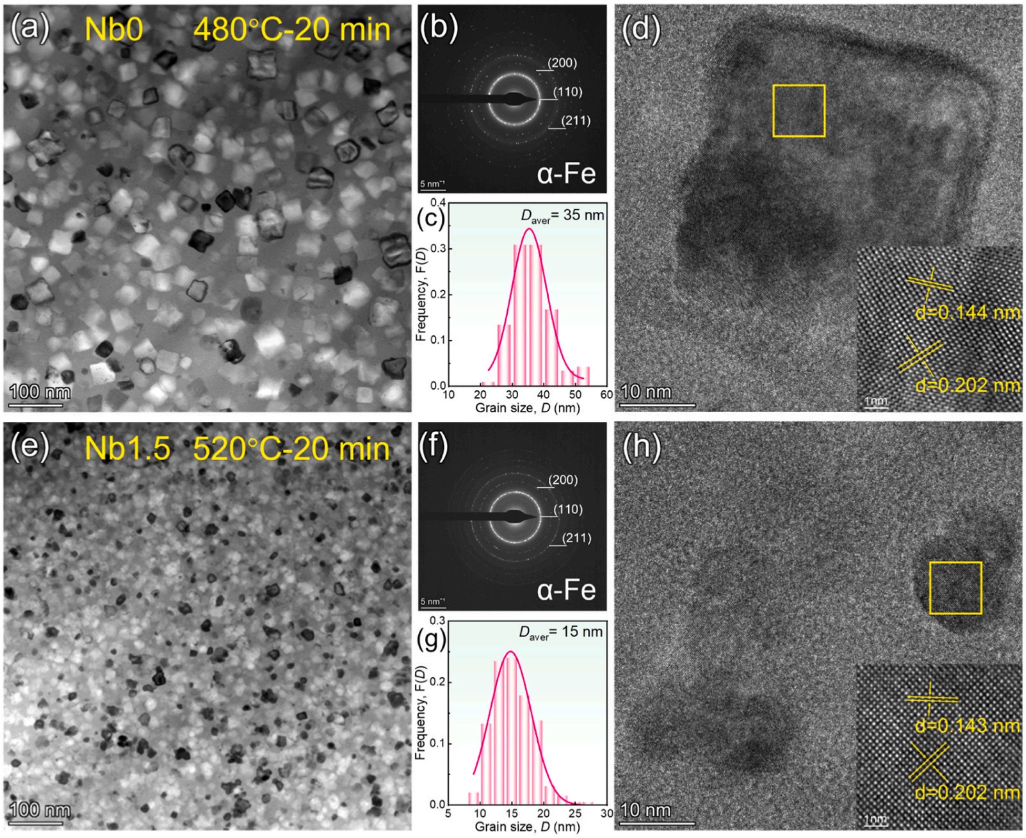

Fig. 9. Bright-field TEM images, corresponding SAED patterns, and grain size distribution of optimally annealed Nb0 (a-c) and Nb1.5 (e-g), respectively. HRTEM image of optimally annealed Nb0 (d) and Nb1.5 (h), with the insets showing the inverse Fourier transform of yellow square areas in (d) and (h), respectively.

grains uniformly distributed in the amorphous matrix (Fig. 9**(e)**), and the average grain size is only 15 nm (Fig. 9**(g)**). Moreover, the V_{cr} was significantly increased, which is consistent with the results in Table 2. High-resolution TEM images of Nb1.5 (Fig. 9**(h)**) show that the precipitated nanocrystals are equiaxed grains with good roundness, which are obviously different from the square nanograin in Fig. 9**(d)**. In addition, the inverse Fourier transform (IFT) images reveal a regularly arranged fringe contrast of bcc (110) and (200) planes, indicating the absence of internal defects in the α-Fe precipitation phase [36]. From the IFT analysis, the interplanar spacing for Nb1.5 is determined to be 0.202 and 0.143 nm for the (110) and (200) planes, respectively. Similar spacings are observed for the Nb0 alloy ribbons. These results suggest that the addition of Nb does not alter the microstructure of the α-Fe phase and its inherent soft magnetic properties [7].

According to Herzer's random anisotropy model [37], when α-Fe grain size (D) is smaller than the ferromagnetic exchange correlation length (20–40 nm), the local magneto-crystalline anisotropy (K_1) is averaged out due to the exchange interactions, thereby reducing the effective anisotropy constant $<K>$. The model predicts that $<K>$ varies strongly with grain size (D^6). However, this model does not consider the role of the residual amorphous phase, and hence, it is not strictly applicable to the variety of unique magnetic behaviors that arise from the two-phase nature [35]. In the two-phase nanocrystalline soft magnetic alloy, Suzuki et al. developed a two-phase random anisotropy model. The effective magnetocrystalline anisotropy can be written as [35]:

$$\langle K\rangle \approx \frac{1}{\varphi^6}(1-V_{am})^4 K_1^4\left(\frac{D}{\sqrt{A_{cr}}}+\frac{\Lambda}{\sqrt{A_{am}}}\right)^6 \tag{5}$$

where φ is the spin rotation angle over the exchange-correlation length, V_{am} is the amorphous volume fraction, A_{am} and A_{cr} are exchange stiffness of amorphous and crystalline phases, respectively. It can be seen that $<K>$ is proportional to D^6 and Λ^6 from Eq. (5). Therefore, when the values of D and Λ decrease, the $<K>$ value decreases accordingly. To understand such significant variation in detail, the initial magnetization curves of the Nb0 and Nb1.5 alloys (Fig. 10**(a)**) were measured. The effective magnetic anisotropy $<K>$ can be determined by means of the law of approach to saturation [38,39].

$$M = M_s\left(1-\frac{a}{H}-\frac{b}{H^2}-\ldots\right)+\chi_p H \tag{6}$$

$$\chi = \frac{dM}{dH} = M_s\left(\frac{a}{H^2}+\frac{2b}{H^3}+\ldots\right)+\chi_p \tag{7}$$

$$\langle K\rangle = \frac{1}{2}\mu_0 M_s\sqrt{15b} \tag{8}$$

where M_s is the saturation magnetization, a and b are related to structural inhomogeneity and magneto-crystalline anisotropy, χ_p is the magnetic susceptibility of paraprocess of spins, and μ_0 is the free-space magnetic permeability. Fig. 10(a) shows the initial magnetization curves of the optimally annealed Nb0 and Nb1.5 alloys. The susceptibility χ at various H can then be obtained and plotted as χ versus H^{-3} curve (Fig. 10(b)). Since the term a/H^2 is only significant at low fields, the approaching saturation region is dominated by the term $2b/H^3$. In this range, χ increases linearly with H^{-3}, and the slope of this linear part is B. Using the relation $B = 2bM_s$ and Eq. (8), the value of $<K>$ can be obtained. By using the least square method, we find that the slopes of the line are 4.62×10^9 and 3.85×10^8 $(A/m)^3$ for the Nb0 and Nb1.5, respectively. Consequently, the $<K>$ are calculated to be 127 and 35 J/m^3, respectively. Coercivity and initial permeability are closely related to $<K>$ by

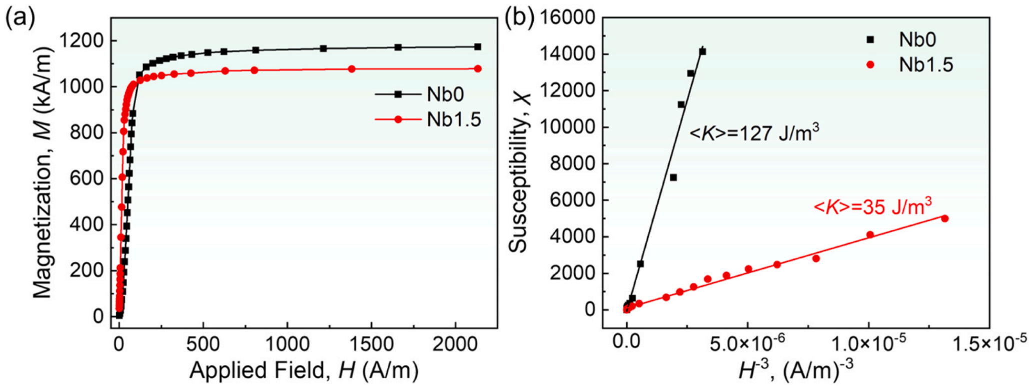

Fig. 10. (a) Initial magnetization curves of the optimally annealed Nb0 and Nb1.5, and (b) corresponding $\chi - H^{-3}$ curves showing the approaching saturation magnetization.

$$H_c = P_c \frac{\langle K \rangle}{J_s}, \mu_i = P_\mu \frac{J_s^2}{\mu_0 \langle K \rangle} \tag{9}$$

where J_s is the average saturation polarization, P_c and P_μ are dimensionless pre-factors of the order of unity and μ_0 is the vacuum permeability. Accordingly, coercivity is proportional to $<K>$, whereas permeability is inversely proportional to $<K>$. For the Nb0 alloy ($D =$ 35 nm, Λ= 14.9 nm), the large grain size and amorphous layer thickness result in ineffective averaging of K_1, leading to inferior soft magnetic properties. By contrast, the Nb1.5 alloy ($D = 15$ nm, Λ= 3.3 nm) exhibits significantly improved soft magnetic properties due to enhanced grain refinement that promotes an effective average of K_1 that leads to a low $<K>$. Furthermore, the reduced Λ and improved microstructure uniformity in Nb-containing alloys enhance intergranular exchange coupling, thereby further contributing to increased magnetic softness.

3.4. Magnetic domain structure

To gain deeper insight into soft magnetic properties, the magnetic domain structure in zero magnetic field (demagnetized state) of Nb0 and Nb1.5 alloys annealed at optimized temperatures was analyzed, as shown in Fig. 11. It is known that magnetic domains are associated with magnetic anisotropies and reflect the configuration of spins. They are formed to minimize the total magnetic Gibbs free energy, which consists of magnetostatic stray field energy, anisotropy energy, and domain wall energy [40,41]. If the spontaneous magnetization tends to orient along the ribbon plane (tensile stress), then magnetostatic stray field energy and anisotropy energy become the lowest which leads to the formation of wide domain structure. However, when the anisotropy axis is perpendicular to the ribbon plane (compressive stress) a closure domain structure needs to appear to minimize magnetostatic stray field energy. The as-quenched (AQ) sample exhibits curved strip magnetic domains, along with small-scale mazing patterns, as shown in Figs. 11**a** and 11**c**. These mazing patterns are a characteristic manifestation of stress-induced closure domains [42,43]. For annealed Nb0 alloy samples, the stress-induced mazing domains vanished, and exhibited wide strip domains (Fig. 11**b**). However, due to its large grain size, the K_1 remains insufficiently averaged, resulting in significant magnetic anisotropy (127 J/m^3). This anisotropy, in turn, causes the bending of the domain walls and the emergence of pinning sites (Pinning domain walls), all of which degrade the soft magnetic properties. In contrast, the Nb1.5 alloy (Fig. 11**d**) domain pattern displays smooth-edged and

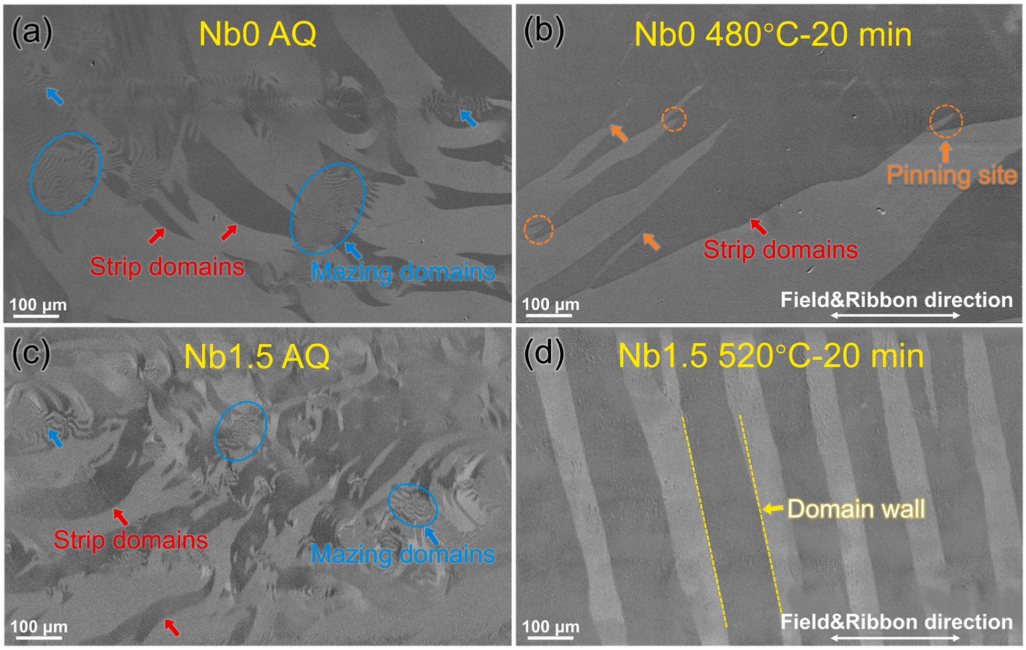

Fig. 11. Magnetic domain structure of Fe$_{76.3\text{-}x}$Si$_9$B$_{10}$P$_4$Cu$_{0.7}$Nb$_x$ (x = 0 and 1.5) alloy ribbons in the as-quenched and optimized annealed state. (a, b) Nb0; (c, d) Nb1.5.

wide-stripe domains, indicating a lower pinning effect and reduced anisotropy (35 J/m^3), consistent with the trends observed in H_c, μ_e and P_{cm}.

4. Conclusions

This study systematically investigated the effects of Nb addition on the thermal stability, AFA, microstructural evolution and soft magnetic properties of the $Fe_{76.3\text{-}x}Si_9B_{10}P_4Cu_{0.7}Nb_x$ alloy. The key findings are summarized as follows:

(1) Increasing Nb content leads to higher onset crystallization temperatures (T_{x1} and T_{x2}), with an enlarged temperature interval ($\Delta T = T_{x2}\text{-}T_{x1}$), primarily due to the pronounced rise in T_{x2}, which facilitates the homogeneous precipitation of α-Fe nanocrystals.
(2) The supercooled liquid region ($\Delta T_x = T_x\text{-}T_g$) increases from 43 °C (Nb0) to 70 °C (Nb1.5), indicating improved AFA with increasing Nb content.
(3) Nb addition effectively refines the grain size and increases the crystallization volume fraction of the α-Fe(Si) phase, significantly reducing magnetic anisotropy and optimizing the magnetic domain structure.
(4) As the Nb content increases, the B_s decreases monotonically from 1.48 T to 1.32 T. The H_c decreases sharply from 9.6 A/m (Nb0) to 1.75 A/m (Nb1.5).
(5) The Nb1.5 alloy exhibits the most favorable combination, with $B_s = 1.36$ T, $\mu_{e\ (1\ kHz)} = 19400$, $H_c = 1.75$ A/m, and P_{cm} (0.2 T, 20 kHz) = 4.94 W/kg. The synergy of excellent thermal stability and superior soft magnetic properties makes this alloy a promising candidate for industrial applications.

CRediT authorship contribution statement

Changlong Jin: Investigation, Data curation. **Min Wang:** Investigation, Data curation. **Yanzhou Fan:** Writing – original draft, Investigation, Formal analysis, Data curation. **Baolong Shen:** Writing – review & editing, Supervision, Project administration, Funding acquisition. **Qiang Luo:** Formal analysis. **Zhijun Guo:** Writing – review & editing, Methodology, Funding acquisition. **Dong Li:** Investigation. **Jifeng Zhou:** Formal analysis. **Jinhong Fu:** Investigation.

Declaration of Competing Interest

The authors declare that they have no known competing financial interests or personal relationships that could have appeared to influence the work reported in this paper.

Acknowledgments

This work was financially supported by the National Key R&D Program of China (No. 2022YFB3804100), the National Natural Science Foundation of China (No. 52231005), the Science Technology Development Program of Yixing (No. C2024002).

Appendix A. Supporting information

Supplementary data associated with this article can be found in the online version at doi:10.1016/j.jallcom.2025.184627.

Data availability

Data will be made available on request.

References

[1] J.M. Silveyra, E. Ferrara, D.L. Huber, T.C. Monson, Soft magnetic materials for a sustainable and electrified world, Science 362 (2018) eaao0195.
[2] S.Y. Yang, B.W. Zang, M.L. Xiang, F.Y. Shen, L.J. Song, M. Gao, Y. Zhang, J.T. Huo, J.Q. Wang, Designing Fe-based amorphous alloys with both ultra-high magnetization and ultra-low coercivity through artificial intelligence, Adv. Funct. Mater. (2025) 2425588.
[3] X.S. Li, J. Zhou, L.Q. Shen, B.A. Sun, H.Y. Bai, W.H. Wang, Exceptionally high saturation magnetic flux density and ultralow coercivity via an amorphous-nanocrystalline transitional microstructure in an FeCo-based alloy, Adv. Mater. 35 (2022) e2205863.
[4] M. Jiang, M. Cai, J. Zhou, S. Di, X. Li, Q. Luo, B. Shen, Superior high-frequency performances of Fe-based soft-magnetic nanocrystalline alloys, Mater. Today Nano 22 (2023) 100307.
[5] L. Hou, W.M. Yang, Q. Luo, X.D. Fan, H.S. Liu, B.L. Shen, High B_s of FePBCCu nanocrystalline alloys with excellent soft-magnetic properties, J. Non-Cryst. Solids 530 (2020) 119800.
[6] C.R. Wang, Y.H. Li, B.S. Li, L. Jiang, T.C. Liu, W. Zhang, Optimizing structure and magnetic softness of low-Nb-content Fe-Si-B-Nb-Cu nanocrystalline alloys by regulating Si/B ratio and Cu content, Mater. Today Commun. 40 (2024) 110043.
[7] Y.L. Li, Z.X. Dou, X.M. Chen, K. Lv, F.S. Li, X.D. Hui, Improving the amorphous forming ability and magnetic properties of FeSiBPCu amorphous and nanocrystalline alloys by utilizing carbon, J. Alloy Compd. 844 (2020) 155767.
[8] F.P. Wan, A.N. He, J.H. Zhang, J.C. Song, A.D. Wang, C.T. Chang, X.M. Wang, Development of FeSiBNbCu nanocrystalline soft magnetic alloys with high B_s and good manufacturability, J. Electron. Mater. 45 (2016) 4913–4918.
[9] A. Makino, H. Men, T. Kubota, K. Yubuta, A. Inoue, New excellent soft magnetic FeSiBPCu nanocrystallized alloys with high B_s of 1.9 T from nanohetero-amorphous phase, IEEE Trans. Magn. 45 (2009) 4302–4305.
[10] T. Kubota, A. Makino, A. Inoue, Low core loss of $Fe_{85}Si_2B_8P_4Cu_1$ nanocrystalline alloys with high B_s and B_{800}, J. Alloy Compd. 509 (2011) S416–S419.
[11] T. Liu, A.D. Wang, C.L. Zhao, S.Q. Yue, X.M. Wang, C.T. Liu, Compositional design and crystallization mechanism of high B_s nanocrystalline alloys, Mater. Res. Bull. 112 (2019) 323–330.
[12] P. Sharma, X. Zhang, Y. Zhang, A. Makino, Competition driven nanocrystallization in high B_s and low coreloss Fe-Si-B-P-Cu soft magnetic alloys, Scr. Mater. 95 (2015) 3–6.
[13] C.T. Chang, Z. Xiang, C.L. Zhao, A.D. Wang, R.R. Song, D. Pan, Enlarging heat-treatment processing windows of Fe-Si-B-P-Cu-M nanocrystalline alloys by doping transition metal elements, J. Alloy Compd. 860 (2021) 158420.
[14] M. Ohta, Y. Yoshizawa, High B_s nanocrystalline $Fe_{84\text{-}x\text{-}y}Cu_xNb_ySi_4B_{12}$ alloys (x=0.0-1.4, y=0.0-2.5), J. Magn. Magn. Mater. 321 (2009) 2220–2224.
[15] X.J. Jia, Y.H. Li, G.Q. Xie, T.L. Qi, W. Zhang, Role of Mo addition on structure and magnetic properties of the $Fe_{85}Si_2B_8P_4Cu_1$ nanocrystalline alloy, J. Non-Cryst. Solids 481 (2018) 590–593.
[16] R.B. Wang, L.X. Shi, Y. Wu, J.L. Jia, Y. Shao, K.F. Yao, Effects of Mo on the glass forming ability and properties of Fe-B-C-P-Si-Mo bulk metallic glasses, J. Non-Cryst. Solids 629 (2024) 122868.
[17] J.M. Park, J.S. Park, D.H. Kim, J.H. Kim, E. Fleury, Formation, and mechanical and magnetic properties of bulk ferromagnetic Fe-Nb-B-Y-(Zr, Co) alloys, J. Mater. Res. 21 (2006) 1019–1024.
[18] X. Wang, Q. Wang, B.Z. Tang, D. Ding, L. Cui, L. Xia, Effect of Mn substitution Fe on the formability and magnetic properties of amorphous $Fe_{88}Zr_8B_4$ alloy, Metals 11 (2021) 1577.
[19] X. Li, C.T. Chang, T. Kubota, C.L. Qin, A. Makino, A. Inoue, Effect of Cr addition on the glass-forming ability, magnetic, mechanical and corrosion properties of $(Fe_{0.76}Si_{0.096}B_{0.096}P_{0.048})_{100\text{-}x}Cr_x$ bulk glassy alloys, Mater. Trans. 49 (2008) 2887–2890.
[20] J. Xiong, B.W. Bai, H.R. Jiang, A. Faus-Golfe, Determinants of saturation magnetic flux density in Fe-based metallic glasses: insights from machine-learning models, Rare Met. 43 (2024) 5256–5267.
[21] H.R. Lashgari, D. Chu, S.S. Xie, H.D. Sun, M. Ferry, S. Li, Composition dependence of the microstructure and soft magnetic properties of Fe-based amorphous/nanocrystalline alloys: a review study, J. Non-Cryst. Solids 391 (2014) 61–82.
[22] H.Z. Fang, X.D. Hui, G.L. Chen, Effects of Mn addition on the magnetic property and corrosion resistance of bulk amorphous steels, J. Alloy Compd. 464 (2008) 292–295.
[23] Z. Xiang, A.D. Wang, C.L. Zhao, H. Men, X.M. Wang, C.T. Chang, D. Pan, Optimization of thermal stability and soft-magnetic properties of FeSiBPCuNb alloys by Nb content tuning, J. Alloy Compd. 622 (2015) 1000–1004.
[24] Y.Z. Fan, Z.J. Guo, M. Wang, C.L. Jin, J.F. Zhou, Y.Q. Dong, Q.K. Man, B.L. Shen, Phosphating-enhanced Fe-based amorphous soft magnetic composites with ultra-low power loss for efficient electrical energy conversion, Sci. China: Phys., Mech. Astron. 68 (2025) 106112.
[25] C.C. Cao, L. Zhu, Y. Meng, X.B. Zhai, Y.G. Wang, Atomic level structural modulation during the structural relaxation and its effect on magnetic properties of $Fe_{81}Si_4B_{10}P_4Cu_1$ nanocrystalline alloy, J. Magn. Magn. Mater. 456 (2018) 274–280.
[26] K.L. Alvarez, J.M. Martín, N. Burgos, M. Ipatov, L. Domínguez, J. González, Structural and magnetic properties of amorphous and nanocrystalline Fe-Si-B-P-Nb-Cu alloys produced by gas atomization, J. Alloy Compd. 810 (2019) 151754.
[27] Y.L. Li, N.N. Shen, S. Zhang, Y.D. Wu, L. Chen, K. Lv, Z.B. He, F.S. Li, X.D. Hui, Crystallization behavior and soft magnetic properties of Fe-B-P-C-Cu ribbons with amorphous/α-Fe hierarchic structure, Intermetallics 131 (2021) 107100.

[28] A. Inoue, Bulk amorphous alloys with soft and hard magnetic properties, Mater. Sci. Eng. A 226 (228) (1997) 357–363.
[29] L.X. Shi, K.F. Yao, Composition design for Fe-based soft magnetic amorphous and nanocrystalline alloys with high fe content, Mater. Des. 189 (2020) 108511.
[30] K. Hono, D.H. Ping, M. Ohnuma, H. Onodera, Cu clustering and Si partitioning in the early crystallization stage of an $Fe_{73.5}Si_{13.5}B_9Nb_3Cu_1$ amorphous alloy, Acta Mater. 47 (1999) 997–1006.
[31] Y. Yoshizawa, S. Oguma, K. Yamauchi, New Fe-based soft magnetic alloys composed of ultrafine grain structure, J. Appl. Phys. 64 (1988) 6044–6046.
[32] X. Jia, Y. Dong, L. Zhang, Y. Li, A. He, J. Li, Influence of static magnetic field on rapid solidified structure and nanocrystallization behavior of Fe-Si-B-Cu soft magnetic alloys with pre-existing α-Fe nanocrystals, J. Mater. Res. Technol. 24 (2023) 9594–9600.
[33] X.D. Fan, T. Zhang, M.F. Jiang, W.M. Yang, B.L. Shen, Synthesis of novel FeSiBPCCu alloys with high amorphous forming ability and good soft magnetic properties, J. Non-Cryst. Solids 503-504 (2019) 36–43.
[34] C. Wu, H.P. Chen, H.P. Lv, M. Yan, Interplay of crystallization, stress relaxation and magnetic properties for FeCuNbSiB soft magnetic composites, J. Alloy Compd. 673 (2016) 278–282.
[35] K. Suzuki, J.M. Cadogan, Random magnetocrystalline anisotropy in two-phase nanocrystalline systems, Phys. Rev. B 58 (1998) 2730–2739.
[36] L.L. Pang, A. Inoue, E.N. Zanaeva, F. Wang, A.I. Bazlov, Y. Han, F.L. Kong, S.L. Zhu, R.B. Shull, Nanocrystallization, good soft magnetic properties and ultrahigh mechanical strength for $Fe_{82\text{-}85}B_{13\text{-}16}Si_1Cu_1$ amorphous alloys, J. Alloy Compd. 785 (2019) 25–37.
[37] G. Herzer, Modern soft magnets: amorphous and nanocrystalline materials, Acta Mater. 61 (2013) 718–734.
[38] K.Y. Ho, X.Y. Xiong, J. Zhi, L.Z. Cheng, Measurement of effective magnetic anisotropy of nanocrystalline Fe-Cu-Nb-Si-B soft magnetic alloys, J. Appl. Phys. 74 (1993) 6788–6790.
[39] K.B. Wang, C. Wu, L.F. Wang, X.Y. Zhang, Q.M. Chen, M. Yan, Deep supercooling solidification towards tuned amorphous/nanocrystalline dual phases for superior magnetic nanocrystalline alloys, Mater. Des. 248 (2024) 113469.
[40] L.Q. Shen, P. Luo, Y.C. Hu, H.Y. Bai, Y.H. Sun, B.A. Sun, Y.H. Liu, W.H. Wang, Shear-band affected zone revealed by magnetic domains in a ferromagnetic metallic glass, Nat. Commun. 9 (2018) 4414.
[41] S. Mallick, P. Sharma, K. Takenaka, A. Makino, S. Bedanta, Static and dynamic behavior of domain walls in high B_s soft magnetic ribbons tuned by the annealing temperature, J. Phys. D Appl. Phys. 51 (2018) 065007.
[42] J.F. Li, I.V. Soldatov, X.C. Tang, B.Y. Sun, R. Schafer, S.L. Liu, Y.Q. Yan, H.B. Ke, Y. H. Sun, J. Orava, H.Y. Bai, Metallic mimosa pudica: a 3D biomimetic buckling structure made of metallic glasses, Sci. Adv. 8 (2022) eabm7658.
[43] H.Y. Xiao, A.D. Wang, J.W. Li, A.N. He, T. Liu, Y.Q. Dong, H. Guo, X.C. Liu, Structural evolutionary process and interrelation for FeSiBNbCuMo nanocrystalline alloy, J. Alloy Compd. 821 (2020) 153487.